



1 **Pronounced impact of salinity on rapidly intensifying tropical cyclones**

2 Karthik Balaguru

3 *Pacific Northwest National Laboratory, Richland, WA, USA*

4 Gregory R. Foltz*

5 *Atlantic Oceanographic and Meteorological Laboratory (NOAA), Miami, FL, USA*

6 L. Ruby Leung

7 *Pacific Northwest National Laboratory, Richland, WA, USA*

8 John Kaplan

9 *Atlantic Oceanographic and Meteorological Laboratory (NOAA), Miami, FL, USA*

10 Wenwei Xu

11 *Pacific Northwest National Laboratory, Richland, WA, USA*

12 Nicolas Reul and Bertrand Chapron

13 *Laboratoire d'Océanographie Physique et Spatiale, Ifremer, Brest, France*

14 *Corresponding author: Gregory R. Foltz, Gregory.Foltz@noaa.gov

Early Online Release: This preliminary version has been accepted for publication in *Bulletin of the American Meteorological Society*, may be fully cited, and has been assigned DOI 10.1175/BAMS-D-19-0303.1. The final typeset copyedited article will replace the EOR at the above DOI when it is published.

ABSTRACT

15 Tropical Cyclone (TC) rapid intensification (RI) is difficult to predict and poses a formidable
16 threat to coastal populations. A warm upper ocean is well-known to favor RI, but the role of ocean
17 salinity is less clear. This study shows a strong inverse relationship between salinity and TC RI
18 in the eastern Caribbean and western tropical Atlantic due to near-surface freshening from the
19 Amazon-Orinoco River system. In this region, rapidly intensifying TCs induce a much stronger
20 surface enthalpy flux compared to more weakly intensifying storms, in part due to a reduction in
21 SST cooling caused by salinity stratification. This reduction has a noticeable positive impact on
22 TCs undergoing RI, but the impact of salinity on more weakly intensifying storms is insignificant.
23 These statistical results are confirmed through experiments with an ocean mixed layer model, which
24 show that the salinity-induced reduction in SST cold wakes increases significantly as the storm's
25 intensification rate increases. Currently, operational statistical-dynamical RI models do not use
26 salinity as a predictor. Through experiments with a statistical RI prediction scheme, it is found
27 that the inclusion of surface salinity significantly improves the RI detection skill, offering promise
28 for improved operational RI prediction. Satellite surface salinity may be valuable for this purpose,
29 given its global coverage and availability in near real-time.

30 *Capsule summary.* We show the importance of salinity for rapidly intensifying Atlantic tropical
31 cyclones and demonstrate the potential for improved prediction of rapid intensification through the
32 inclusion of salinity.

33 **1. Introduction**

34 Rapid intensification (RI) of tropical cyclones (TCs), defined as the 95th percentile of 24-hr
35 over-water intensity changes, or an increase in intensity of at least 30 kt in a 24-hr period, is
36 extremely difficult to predict. The challenge is at the forefront of operational TC forecasting (Gall
37 et al. 2013). Considering that all Category 4 and 5 TCs in the Atlantic undergo RI during their
38 lifetimes (Kaplan and DeMaria 2003), the significance of RI is disproportionately high relative to
39 the low chance of occurrence (Lee et al. 2016). The hyperactive 2017 Atlantic TC season was
40 extremely destructive, with several intense TCs making devastating landfalls after undergoing RI
41 (Rahmstorf 2017; Balaguru et al. 2018; Klotzbach et al. 2018). In 2018, TCs Florence and Michael
42 underwent unanticipated explosive RI in the eastern Atlantic and in the Gulf of Mexico, before
43 impacting the Carolinas and the Florida panhandle, respectively (Avila 2019). More recently, in
44 August 2019 TC Dorian underwent RI to the north of the Caribbean Sea before scything through
45 the Bahamas. With RI of TCs projected to rise in coastal regions just before landfall under climate
46 change (Emanuel 2017), there is a critical need to improve our understanding of the phenomenon.

47 TCs intensify by extracting heat energy from the ocean. Sea surface temperature (SST) under
48 the core of the storm, and processes that govern its evolution, therefore play a critical role in TC
49 intensification (Emanuel 1999; Cione and Uhlhorn 2003). When over the ocean, a TC's intense
50 winds induce vertical mixing and sea surface cooling that acts as a negative feedback on the
51 storm's intensity, causing upper-ocean density stratification to affect the storm's intensification
52 (Price 1981; Bender and Ginis 2000; Cione and Uhlhorn 2003). While some studies suggest that

53 processes typically favoring TC intensification are also responsible for RI (Kowch and Emanuel
54 2015), others indicate that we need to improve our understanding of mechanisms governing RI
55 (Rozoff and Kossin 2011).

56 For operational forecasting of RI, some of the best performing models are statistical (Kaplan et al.
57 2015). In these models, environmental parameters that influence RI are combined using statistical
58 techniques such as linear discriminant analysis, logistic regression, or Bayesian methods in order
59 to predict the chance of RI occurrence (Kaplan et al. 2010; Rozoff and Kossin 2011; Kaplan et al.
60 2015). Typically, SST and Tropical Cyclone Heat Potential (TCHP), metrics for the warmth of
61 the ocean surface and the depth of the warm water reservoir (Shay et al. 2000), respectively, are
62 used to represent the ocean in these models (Kaplan et al. 2010, 2015). Though SST and TCHP
63 include effects of upper-ocean thermal structure, they do not incorporate salinity impacts on ocean
64 stratification (Balaguru et al. 2015). This leads to the following question: Does salinity play a role
65 in RI? In the western tropical Atlantic, near-surface ocean stratification is substantially enhanced
66 by the freshwater lens of the Amazon-Orinoco River system, which acts to inhibit TC-induced
67 oceanic mixing and SST cooling (Balaguru et al. 2012; Grodsky et al. 2012). While several
68 previous studies have shown varying degrees of salinity impact on TC intensification (Balaguru
69 et al. 2012; Grodsky et al. 2012; Reul et al. 2014; Newinger and Toumi 2015; Androulidakis et al.
70 2016; Yan et al. 2017; Rudzin et al. 2019; Hlywiak and Nolan 2019), its specific role in RI has not
71 been evaluated.

72 Irma, the strongest TC from the 2017 Atlantic TC season based on maximum sustained winds,
73 reached a peak intensity of 155 knots and maintained Category 5 strength longer than any other TC
74 in the world (Rahmstorf 2017; Klotzbach et al. 2018). Between September 4 and 6, Irma underwent
75 a phase of RI to the east of the Caribbean Islands before making destructive landfalls in the Leeward
76 Islands of the West Indies, Cuba, and the Florida Keys. The upper-ocean state just before TC Irma

77 formed on August 30 suggests that as the storm moved west of 50°W, it encountered an increasingly
78 favorable ocean (Figs. 1A and 1B). SSTs exceeded 28°C and TCHP was higher than 50 kJ cm⁻²
79 in much of the western Atlantic. The largest values of SST and TCHP, exceeding 29°C and 100 kJ
80 cm⁻² respectively, were found in the northwestern Caribbean Sea and near the entrance to the Gulf
81 of Mexico. The spatial variability of sea surface salinity (SSS), on the other hand, is dominated by
82 the freshwater plume of the Amazon-Orinoco River system, stretching approximately from 50°W
83 to 70°W and from the South American coast to 25°N (Fig. 1C). Irma appears to have traversed the
84 plume when it underwent RI. The storm commenced strengthening just to the west of 50°W and
85 subsequently entered a phase of RI, centered around 55°W, where it increased in intensity from
86 Category 3 to Category 5 (Fig. 1C). During this period, SST and TCHP increased by about 1°C
87 and 30 kJ cm⁻² respectively (Figs. 1D and 1E). However, the TC also encountered nearly a 2 psu
88 drop in salinity between 50°W and 55°W when it underwent RI (Fig. 1F).

89 Matthew, the most powerful TC from the 2016 season (Stewart 2017), also appears to have
90 undergone RI over low-salinity plume waters to the north of Venezuela in the Caribbean Sea (Sup-
91 plementary Fig. 1A and 1B). A brief examination of along-track conditions for Gonzalo (2014), a
92 Category 4 TC that caused widespread destruction in the Leeward Islands and Bermuda, indicates
93 that it also underwent RI while over the freshwater plume near Puerto Rico (Supplementary Fig.
94 1C and 1D; (Domingues et al. 2015)). Similarly, Igor, an intense Category 4 TC from the 2010
95 season likely intensified rapidly over the northern tip of the Amazon River plume (Reul et al. 2014).
96 Hence, this preliminary examination of a few TCs raises the following question: Can the influence
97 of the ocean on RI be attributed mostly to the upper-ocean thermal structure, or does salinity also
98 play an important role? In this study, using a combination of observations and numerical model
99 simulations, we explore the potential role of salinity in RI.

2. Methods

a. Data

Atlantic TC best track data (HURDAT2) for the period 2002-2018, obtained from the National Hurricane Center (<https://www.nhc.noaa.gov>; Landsea and Franklin (2013)), are used to identify storm locations and to derive TC intensification rates. We use daily optimally interpolated SST from Remote Sensing Systems (www.remss.com) for the period 2002-2018 at a 9 km spatial resolution to estimate pre-storm SST (defined as SST three days before the storm's arrival) and TC-induced cold wakes or SST cooling (estimated as the difference between SST on the day of the TC and the pre-storm SST) along the storms' tracks. This product combines data from all available infrared and microwave satellites. Daily objectively analyzed air-sea fluxes (OAFlux, Yu et al. (2008)), obtained from <http://oaflux.whoi.edu> for the period 2002-2018, are used to estimate the enthalpy flux at the air-sea interface under TCs. Enthalpy flux is computed as the sum of latent and sensible heat fluxes on the day of the TC. Although the product is available at a spatial resolution of 1°, it has been used to understand air-sea heat fluxes under TCs previously (Balaguru et al. 2012). All data are obtained beginning in 2002, when the satellite-based Remote Sensing Systems SST data are made available.

Along-track TCHP is calculated using vertical ocean temperature profiles from HYCOM Global Ocean Forecast System version 3.1 reanalysis (Chassignet et al. 2007). In addition to TCHP, pre-storm ocean temperature and salinity profiles are used to calculate ocean density, temperature, and salinity stratification along TC tracks. HYCOM reanalysis is available at 3-hourly frequency and at an eddy-resolving 8 km spatial resolution from <https://www.hycom.org>. The vertical resolution in the upper 100 m varies from 2-10 m, with higher resolution close to the surface. We extract data at daily frequency for our calculations. As for pre-storm SST, various parameters are obtained from

123 HYCOM three days before the storm's arrival. To validate our main results based on HYCOM,
124 we use vertical ocean temperature and salinity profiles from version 3.4.2 of the Simple Ocean
125 Data Assimilation (SODA) reanalysis (Carton et al. 2018), available at a 0.5° spatial resolution and
126 as 5-day means from <http://www.soda.umd.edu>. In the upper 100 m, the vertical resolution
127 is approximately 10 m. TCHP, ocean stratification, and SSS are obtained from SODA over the
128 5-day period prior to the storm's arrival. The HYCOM and SODA 3.4.2 reanalyses are available
129 for the periods 1994–2015 and 1980–2017, respectively. In this study, data are used beginning in
130 2004 since the availability of Argo floats makes estimates of the ocean subsurface more reliable
131 over this period (Baker et al. 2019). 9-day mean SSS measurements from the Soil Moisture and
132 Ocean Salinity (SMOS) satellite (Boutin et al. 2017), available from <http://www.catds.fr> at
133 a resolution of 0.25° and for the period 2010–2017, are used to estimate pre-storm ocean salinity
134 along TC tracks. These data are used to provide an independent validation of HYCOM, and to
135 show the potential value of satellite SSS for prediction. Pre-storm SSS is calculated as the SSS
136 averaged over the 9-day period prior to the storm. Note that the time periods for various datasets
137 differ slightly in order to maximize the data used for different analyses.

138 We explore the impact of salinity on vertical mixing and thus TC-induced SST cooling by
139 using the Price-Weller-Pinkel (PWP) one-dimensional ocean mixed layer model (Price et al. 1986).
140 Model input data are comprised of 20 Argo float temperature and salinity profiles within the region
141 70°W – 50°W , 10°N – 20°N during August–October 2016–2018 (Section 2c).

142 Developmental data for various predictors of the Statistical Hurricane Intensity Prediction
143 Scheme Rapid Intensification Index (SHIPS-RII) were obtained from [http://rammb.cira.
144 colostate.edu/research/tropical_cyclones/ships/developmental_data.asp](http://rammb.cira.colostate.edu/research/tropical_cyclones/ships/developmental_data.asp).

145 These data describe the large-scale TC environment and are derived from gridded operational

146 global analyses (DeMaria et al. 2005). We combine these developmental data and salinity with a
147 statistical model (section 2d) to understand the value of salinity for predicting RI.

148 *b. Calculations*

149 TCHP is calculated as the integral of the temperature from the surface to the depth of the 26°C
150 isotherm:

$$TCHP = \rho C_p \int_0^{Z_{26}} (T(z) - 26) dz \quad (1)$$

151 where ρ is the seawater density, C_p is the seawater specific heat capacity, $T(z)$ is the seawater
152 temperature as a function of water depth, and Z_{26} is the depth of the 26°C isotherm (Shay et al.
153 2000). Temperature, salinity, and density stratification are defined as the difference between the
154 respective variable at a depth of 100 m and the surface value. The above calculations are performed
155 using data from HYCOM and SODA. Track locations contaminated with land effects are excluded
156 from our analysis. Intensity change over a period is calculated as the difference between the
157 intensity at the end of that period and the initial intensity.

158 *c. PWP model experiments*

159 The forcings for the PWP model are the surface heat and moisture fluxes, which here are set to
160 zero throughout the model integrations, and wind stress (Balaguru et al. 2015). The model's mixed
161 layer entrains successively deeper water until the bulk Richardson number exceeds 0.65. Vertical
162 mixing is then performed beneath the mixed layer until the gradient Richardson number between
163 each level is greater than 0.25.

164 The model was initialized with vertical profiles of temperature and salinity from Argo floats
165 in the western tropical Atlantic and eastern Caribbean Sea (50°W–70°W, 10°N–20°N) during

166 August–October 2016–2018. Based on a decorrelation length scale for salinity in the western
167 tropical Atlantic of about 3° (Sena Martins et al. 2015), we chose 20 profiles to approximately
168 represent the range of salinity conditions found in this region. Most of the 20 included profiles
169 exhibit strong salinity stratification in the upper 50 m. Two sets of experiments were conducted,
170 each initialized with one of the 20 Argo profiles. The first set of experiments was initialized with
171 observed temperature and salinity, the second with observed temperature and vertical mean salinity
172 at every depth. In addition, we varied the model’s wind forcing to test the impact of intensification
173 rate on salinity-induced SST cooling as described below.

174 The model was forced with winds from TCs with idealized surface circulations: The surface wind
175 field was assumed to be axisymmetric, with the wind speed a function only of the storm’s maximum
176 wind speed, radius of maximum winds (r_m), and distance from the storm’s center (DeMaria 1987)
177 as follows

$$V(r) = V_m \left(\frac{r}{r_m} \right) \exp \left[\frac{1}{b} \left(1 - \frac{r}{r_m} \right)^b \right] \quad (2)$$

178 Here, $V(r)$ is the tangential wind as a function of distance ‘ r ’ from the storm center and r_m is the
179 radius of maximum tangential winds (V_m). We used a constant value of 0.9 for b in this equation,
180 giving a radius of 23 kt (12 m s^{-1}) winds of ~ 200 km. For all simulations, a r_m of 50 km was used.
181 With these parameters and the storm’s translation speed of 5 m s^{-1} (9.7 kt), the wind speed was
182 calculated as a function of time along a north-south axis running through the storm’s center while
183 accounting for the translation velocity. As the storm moves northward, the wind speed therefore
184 increases from 25 kt to $w_{tot} = \sqrt{w^2 + 9.7^2}$ as the northern eyewall passes, where w is the storm’s
185 maximum rotational wind speed in kt and w_{tot} is the vector sum of the maximum rotational velocity
186 and translation velocity. The wind speed then goes to zero in the eye and back up to w_{tot} in the
187 southern eyewall, here referred to as the second r_m .

188 We performed a control simulation in which the maximum wind was set to 60 kt, the approximate
189 mean intensity of all TCs in the western tropical Atlantic (60°W–100°W, 10°N–30°N). We then
190 conducted an experiment in which the wind profile was decreased linearly along the track (starting
191 with no change at $t=0$) so that the maximum wind speed at the second r_m , located 250 km, or about
192 14 hours, from the start of the integration, was 40 kt. A similar experiment was conducted so that
193 the maximum wind speed at the second r_m was 20 kt. The percentage reduction in wind speed was
194 held constant from the second r_m until the end of the integration time period, which was 24 hours.
195 Similar experiments were performed in which the maximum wind was increased to either 80 kt or
196 100 kt. In total, 200 model runs were performed (20 different initial profiles, each with observed
197 and vertical mean salinity, and for five different TC wind scenarios).

198 *d. Significance of salinity for RI prediction*

199 To quantify the relevance of salinity for RI, we perform binary classification using the statis-
200 tical scheme of Logistic Regression. A statistical binary classification model combines several
201 parameters to predict a binary dependent variable, which in this case is the occurrence of RI. The
202 SHIPS-RII predictors used are: Previous 12-hr intensity change or persistence (PER), 850-200
203 hPa vertical wind shear within a 500 km radius after vortex removal (SHRD), 200 hPa divergence
204 within a 1000 km radius (D200), Percent areas with Total Precipitable Water < 45 mm within a
205 500 km radius and ± 45 degrees of the upshear SHIPS wind direction (TPW), Second principle
206 component of GOES-IR imagery within a 440 km radius (PC2), Standard deviation of GOES-
207 IR brightness temperature within a 50-200 km radius (SDBT), Potential Intensity (POT), TCHP,
208 Inner-core dry-air predictor (ICDA), and Initial intensity (VMX0) (Kaplan et al. 2015). These 10
209 predictors are available for each 6-hourly TC track location. Among them, SHRD, D200, POT,
210 TCHP, and ICDA are averaged over the 24-hr forecast period (Kaplan et al. 2015). Two sets of

211 predictions are performed: one using only these 10 predictors, the other including SSS as an
212 additional predictor.

213 First we divide the dataset, which contains the various SHIPS-RII predictors and SSS estimated
214 for the corresponding 6-hourly locations, into two subsets: one for cases in which TCs underwent
215 RI and another for cases in which TCs did not undergo RI. Next we choose fractions of the data
216 from the two subsets (specified later in this section) and combine them into the training set. The
217 remaining data from the two subsets are then combined into a test set. We train the classification
218 model on the training set and use the trained model to make predictions for the test set.

219 Based on the predictions for the test set, we estimate the skill of the model using four different
220 metrics: Probability of Detection (POD), False Alarm Ratio (FAR), Area Under the Receiver
221 Operating Characteristic (AUROC) and the Brier Score (BS). A True Positive (TP) is defined as a
222 situation when the model correctly predicts the occurrence of RI. A True Negative (TN) is defined
223 as a situation when the model correctly predicts the non-occurrence of RI. A False Positive (FP)
224 is defined as an event where the model incorrectly predicts that an RI will occur, while a False
225 Negative (FN) is defined as an event where the model incorrectly predicts that an RI will not
226 occur. With these definitions, the various metrics used to assess the model ([http://www.cawcr.
227 gov.au/projects/verification/](http://www.cawcr.gov.au/projects/verification/)) are calculated as follows. The POD indicates the number
228 of correctly predicted RI events out of the total number of actual RI events ($\frac{TP}{TP+FN}$). The FAR
229 represents the number of times RI was wrongly predicted to occur out of the total number of times
230 the model predicted RI ($\frac{FP}{TP+FP}$). AUROC, obtained by plotting the False Positive Rate ($\frac{FP}{FP+TN}$)
231 on the x-axis and the True Positive Rate (POD) on the y-axis, represents the ability of the model to
232 separate the occurrence and non-occurrence of RI. Finally, the BS is estimated as the mean squared
233 difference between predicted probabilities and actual outcomes (Wilks 2011). Higher values of
234 POD and AUROC, and lower values of FAR and BS indicate more skill.

235 To test model sensitivity, we use three different fractions of the data for the training set (55%,
236 60% and 65%). In each case, we first use the various SHIPS-RII predictors as features to make
237 predictions. Next, we include SSS along with those predictors to predict RI. All features are
238 scaled between 0 and 1 before use in the model (Kaplan et al. 2010). If the inclusion of SSS
239 increases the POD and AUROC, and decreases the FAR and BS, then salinity is said to have
240 improved the model performance. A Student's t-test for difference of means is used to ascertain the
241 statistical significance of the improvement in prediction. The Logistic model has been implemented
242 using the 'Scikit-learn' machine learning library in Python programming language ([http://](http://scikit-learn.org)
243 scikit-learn.org). When implementing the model, we use the condition that the class-weights
244 are 'balanced,' which ensures that the weights are inversely proportional to the class frequencies.
245 In other words, the model is penalized more when it fails to predict an RI event when compared
246 to a non-RI event. Using this approach allows the model to be trained for handling relatively rare
247 events such as RI.

248 We first use the SHIPS-RII predictors along with SSS from HYCOM for the 12-year period
249 2004-2015. Next, to assess the value of satellite salinity for RI prediction, and to serve as an
250 independent validation, we perform the same analysis using salinity from SMOS for the period
251 2010-2017.

252 **3. Results**

253 We begin by examining the role of the ocean in TC intensification, focusing on RI. The domain
254 of analysis is the region from 40°W to 100°W and from 10°N to 30°N. Nearly 90% of all
255 locations where TCs underwent RI during the period 2002-2018 are found in this domain, making
256 it appropriate for our analysis. Fig. 2A shows the anomalous mean pre-storm SSTs, anomalous
257 mean TC cold wakes, and anomalous mean enthalpy fluxes at the air-sea interface for various

258 intensification rate thresholds. For instance, the anomalous mean SST corresponding to a threshold
259 of 5 kt 24 hrs⁻¹ represents the difference between the mean SST for all 6-hourly track locations
260 where the storm intensified by 5 kt or higher in 24 hours and the SST averaged over all 6-hourly
261 track locations. Similarly, the anomalous mean TC cold wake represents the mean SST cooling
262 over all locations where the intensification rate exceeds a value minus the mean SST cooling over
263 all locations. When computing the anomalous mean, we subsample data so that the initial intensity
264 of the storm and its translation speed are statistically indifferent between the two sets. In other
265 words, data are selected such that ranges for storm strength and forward moving speed are similar
266 in the two data sets. Doing so allows us to remove the effects of the storm state and isolate the
267 impacts of the ocean on TC intensification.

268 In general, the role of the ocean increases with the intensification rate of the TC (Fig. 2A), in
269 line with past work (Lloyd and Vecchi 2011). While the anomalous mean enthalpy fluxes are not
270 statistically significant for lower intensification rate thresholds, they are highly significant for larger
271 intensification rate thresholds. For the 25 kt 24 hrs⁻¹ threshold and RI, the anomalous enthalpy
272 fluxes are about 7.5 and 9.5 W m⁻² higher, respectively. This indicates that for RI, the flux of heat
273 from the ocean into the atmosphere becomes more important compared to weaker intensification
274 rates. The enthalpy flux under the TC is critically dependent on the SST under the core of the
275 storm (Cione and Uhlhorn 2003), which is a combination of the pre-storm SST and the sea surface
276 cooling induced by the TC. As expected, the anomalous mean pre-storm SST increases with the
277 TC's intensification rate. The anomalous mean SST is not significantly higher for all intensification
278 rates greater than zero, but for RI the pre-storm SST is about 0.3°C higher on average.

279 Interestingly, the anomalous mean cold wakes become increasingly weaker with increasing
280 intensification rates, as noted in previous studies (Lloyd and Vecchi 2011; Vincent et al. 2014).
281 Note that a positive value for the anomalous mean wake does not indicate SST warming under a

282 TC, but rather that the cold SST wake is weaker when compared to the mean wake. While the
283 anomalous mean wake is not statistically significant for all intensification rates nor the median
284 intensification threshold (greater than or equal to $5 \text{ kt } 24 \text{ hrs}^{-1}$), for RI the anomalous mean cold
285 wakes are significantly weaker by about 0.15°C . Thus, conditions in the ocean subsurface that cause
286 a weakening of the cold TC wake likely play an important role in RI. These differences in cold
287 wakes are likely due to those in upper-ocean stratification because we have subsampled our data
288 to remove the effects of the storm state. Since both the vertical temperature and salinity structure
289 jointly determine the ocean density stratification, it is important to evaluate which parameter
290 dominates. To this end, we predict the upper-ocean density stratification using the normalized
291 temperature and salinity stratification. Based on the regression coefficients (Figs. 2B and 2C), we
292 can divide our domain broadly into two regions: 1) A western region where variability in the ocean
293 thermal structure tends to dominate that in density (70°W – 100°W , 10°N – 30°N), and 2) An eastern
294 region where salinity significantly modulates density stratification (40°W – 70°W , 10°N – 30°N). The
295 western region includes the western Caribbean Sea and the Gulf of Mexico. In this region, warm
296 upper-ocean features such as the Loop Current, and the eddies shed by it, induce variations in the
297 ocean thermal structure. In the eastern region, freshwater outflow from the Amazon-Orinoco River
298 system imposes significant constraints on the near-surface ocean density stratification.

299 To assess the impact of these spatial variations of temperature and salinity on TC RI, we compute
300 TCHP, ocean stratification (density, temperature and salinity) and SSS along TC tracks for each
301 region. We consider two intensification rate threshold scenarios: 1) A median intensification
302 threshold with intensification rates greater than or equal to $5 \text{ kt } 24 \text{ hrs}^{-1}$, and 2) RI. As before, for
303 each threshold, we compute the anomalous mean TCHP, the anomalous mean ocean stratification
304 (density, temperature and salinity) and the anomalous mean SSS. For the western region (Fig. 3A),
305 none of the parameters is statistically significant for the median intensification threshold, indicating

306 the minimal role played by the ocean subsurface for weaker intensification rates. For RI however,
307 TCHP is highly significant and is larger by about 9.6 kJ cm^{-2} on average (Fig. 3B). This increase in
308 significance for TCHP at higher intensification rates is consistent with previous studies (Mainelli
309 et al. 2008; Kaplan et al. 2015). In regions with a deep thermocline and weak vertical temperature
310 gradients, TC-induced mixing brings less cold water into the mixed layer, causing a reduction in the
311 cold wake magnitude and favoring TC intensification. In the Gulf of Mexico for instance, several
312 historical TCs have intensified rapidly over warm Loop Current eddies, such as Opal (1995) and
313 Katrina (2005) (Shay et al. 2000; Mainelli et al. 2008; Lin et al. 2013). Consequently, TCHP has
314 been shown to be a useful metric of the upper-ocean thermal structure for forecasting RI (Mainelli
315 et al. 2008; Kaplan et al. 2010, 2015).

316 In the eastern region, consistent with results from the western region, none of the oceanic
317 parameters is statistically significant for the median intensification threshold (Fig. 3C). Even
318 for RI, the anomalous mean TCHP and temperature stratification are not statistically significant
319 (Fig. 3D). Note, however, that here we are only examining the subsurface—the anomalous mean
320 SST is always significant for RI. The anomalous mean density and salinity stratification are highly
321 significant for RI cases (Fig. 3D). On average, the density and salinity stratification are significantly
322 higher by about 0.18 kg m^{-3} and 0.27 psu respectively. In other words, the difference between
323 the 100 m depth and surface values for density and salinity are larger. Since the anomalous mean
324 temperature stratification is not statistically significant for RI, we can safely attribute the enhanced
325 density stratification during RI events to that in salinity.

326 The mean intensity of weakly intensifying TCs in the western Atlantic is about 20 kt lower than
327 the mean for RI. Hence, mixing is relatively shallow for weakly intensifying TCs. Thus, even in
328 the absence of strong stratification, the cooling induced at the surface is minimal and the ocean
329 subsurface does not play an important role. On the other hand, at high intensification rates such

330 as RI, the mixing extends considerably deeper. In this situation, without strong stratification that
331 can limit mixing, substantial surface cooling tends to occur that can counteract the intensification
332 of the storm. The freshwater plume of the Amazon-Orinoco River system enhances water column
333 stability, reduces the mechanical mixing induced by TCs, and lowers the cold wake magnitude
334 (Balaguru et al. 2012; Grodsky et al. 2012; Reul et al. 2014; Newinger and Toumi 2015; Androul-
335 idakis et al. 2016; Yan et al. 2017; Rudzin et al. 2019; Hlywiak and Nolan 2019). The anomalous
336 mean SSS is significantly lower by 0.32 psu for RI (Fig. 3D), further supporting the idea that much
337 of the salinity stratification encountered during RI is due to the low salinity plume waters at the
338 ocean surface. To test the robustness of our results, we performed similar analyses using the SODA
339 3.4.2 ocean reanalysis. Consistent relationships were obtained between ocean stratification and TC
340 intensification, confirming the data-independence of our main conclusions (Supplementary Fig.
341 2).

342 To further understand the effect of salinity on TC RI, we perform a suite of idealized numerical
343 sensitivity experiments with the PWP one-dimensional ocean mixed layer model. The locations of
344 the 20 different profiles of ocean temperature and salinity that were used to initialize the model are
345 shown in Fig. 4A. All are in the region 50°W–70°W, 10°N–20°N, which is in close proximity to the
346 Amazon-Orinoco plume. We use profiles during the months of August–October, the climatological
347 peak of the Atlantic TC season. An examination of the vertical structure of these profiles reveals
348 the significance of salinity for ocean stratification in this region (Fig. 4B). In many cases, the
349 mixed layer is confined to a depth of 20-30 m, below which salinity increases rapidly, by as much
350 as 3 psu, over a depth of 50-60 m. We subject these profiles to TC winds representing various
351 intensification rates, as shown in Figure 4C. Although a three-dimensional ocean model is needed
352 to reproduce the full impact of the TC on the ocean, the one-dimensional version of the model

353 can reasonably capture the main effects when an ensemble approach is used (Hlywiak and Nolan
354 2019).

355 The time evolution of the difference in the ensemble mean SST between the experiments initial-
356 ized with and without salinity stratification shows that the impact of salinity on SST increases with
357 the intensification rate (Fig. 4D). For the cases with intensification relative to the 60-kt control
358 simulation (purple and black curves in Fig. 4D), the inclusion of salinity reduces the TC-induced
359 SST cooling by about 0.25–0.3°C at hour 18. In contrast, for storms with less intensification (blue
360 and red curves in Fig. 4D) the salinity-induced reduction in SST cooling is about 0.1–0.15°C. The
361 reduction in cooling caused by salinity stratification is about 0.1°C stronger for RI cases (black
362 curve in Fig. 4D) compared to cases with no intensification (green curve in Fig. 4D), consistent
363 with our earlier result (Fig. 2A). These results also indicate that the significance of salinity for RI
364 is not due to co-located temperature features. If this were the case, the differences in SST cooling
365 between the experiments with and without salinity would be close to zero.

366 Statistical RI prediction models have traditionally struggled more in the Atlantic than in some
367 other basins (Kaplan et al. 2015). Since these models do not include a predictor based on salinity,
368 and in light of the results in this study, we performed binary classification using Logistic Regression
369 to evaluate the potential value of salinity for RI prediction. We conducted two sets of experiments.
370 First, we used the various predictors included in SHIPS-RII to train the Logistic model and predict
371 the occurrence of RI. Next, we repeated this analysis with SSS included as an additional predictor.
372 The main idea behind using SSS is to represent the effects of upper-ocean salinity stratification on
373 TC-induced mixing. In the region influenced by the Amazon-Orinoco plume in the western tropical
374 Atlantic, SSS primarily determines near-surface salinity stratification. A correlation between SSS
375 and salinity stratification along TC tracks for the eastern region based on HYCOM data is about

376 0.9, suggesting that the former is a good indicator of the latter. But to what extent does SSS serve
377 as a proxy for ocean density stratification?

378 To understand the connection between SSS and density stratification, we plot the correlation
379 between the two for various minimum-salinity thresholds (Supplementary Fig. 3A). As the SSS
380 threshold increases, the correlation between salinity and stratification decreases. This suggests
381 that variations in SSS more accurately reflect those in density stratification for lower values of
382 SSS and that SSS is a poor predictor of density stratification at higher values. The transition
383 occurs near 36 psu, which approximately represents the boundary of the Amazon-Orinoco River
384 plume (Pailler et al. 1999). Thus, considering only SSS values below about 36 psu could possibly
385 improve the ability of salinity to separate RI from non-RI. To elucidate this point, we compute the
386 means for salinity with and without RI while masking out salinity higher than a certain threshold
387 each time. The plot of t-values for statistical significance of the difference between means shows
388 that the maximum t-value is achieved near a threshold of 36 psu (Supplementary Fig. 3B). This
389 statistical evidence further supports the idea of masking out higher salinity values. Physically, by
390 doing this we allow salinity to vary primarily within the region influenced by the Amazon-Orinoco
391 plume or other such locations with very fresh surface waters. We now use this masked-SSS along
392 with the other SHIPS-RII predictors in the Logistic model. Results reveal that adding SSS to the
393 Logistic model significantly improves its skill (Table 1). The addition of SSS enhances the POD
394 and AUROC, while lowering the FAR and the BS, reinforcing the value of salinity for RI prediction.
395 Similar results are obtained when salinity stratification is used instead of SSS, in agreement with
396 the tight relationship between them in this region. Though we have demonstrated improvement in
397 RI prediction using salinity from both reanalysis and satellite, the relative merits of each deserve
398 further study.

399 **4. Summary and Discussion**

400 The significance of the upper-ocean thermal structure for RI is well-known. Consequently, related
401 metrics such as TCHP have traditionally been used to represent the ocean in statistical RI prediction
402 models. However, the role of salinity in RI is less clear. In this study, using a suite of observations
403 and numerical model simulations, we have shown that salinity plays an important role in RI in the
404 eastern Caribbean Sea and the western tropical Atlantic where the surface salinity and upper-ocean
405 salinity stratification are heavily constrained by the freshwater plume of the Amazon-Orinoco
406 River system. This is unlike the western Caribbean Sea and the Gulf of Mexico where temperature
407 features dominate the ocean's impact on RI. Strong upper-ocean stratification is not particularly
408 important for weaker intensification, where significant vertical mixing and sea-surface cooling do
409 not occur. On the other hand, stratification plays a pivotal role for RI because a substantial increase
410 in mixing and SST cooling are more likely to occur when stratification is weaker. These results are
411 supported by simulations with the PWP ocean mixed layer model, where we demonstrate that the
412 influence of salinity on RI is independent of that of temperature, and that the relevance of salinity
413 for a TC increases with its intensification rate. Finally, we tested the value of surface salinity, a
414 reasonable proxy for upper-ocean salinity stratification in the Amazon-Orinoco plume region, for
415 RI prediction. Results indicate that the use of SSS may significantly improve models' abilities to
416 forecast RI.

417 Efforts to incorporate salinity stratification into metrics of TC-induced SST cooling have been
418 made in the past (Price 2009; Shay and Brewster 2010; Vincent et al. 2012; Balaguru et al. 2015),
419 and the results from this study emphasize the need for continued progress along these lines. SST and
420 sea level derived from satellites are being used for estimation of upper-ocean heat content and RI
421 forecasting (Goni and Trinanes 2003; Shay and Brewster 2010). But satellite salinity observations,

422 which have been available for nearly a decade, have not been used in weather forecasting to date.
423 Near-continuous measurements of SSS are available from the SMOS satellite since May 2010 and
424 from NASA's Soil Moisture Active-Passive mission since April 2015 (Durack et al. 2016). Surface
425 salinity measurements were also available from NASA's Aquarius mission between August 2011
426 and June 2015. Given the strong influence of the Amazon-Orinoco plume in the western Atlantic
427 and eastern Caribbean, we advocate the use of satellite salinity in statistical RI prediction models,
428 based on its prospects for improved forecasts (Table 1).

429 Though ocean reanalyses tend to do well in regions where they can assimilate a lot of in
430 situ observations such as Argo profiles, satellite data can help in other regions where in situ
431 measurements are relatively sparse (Tranchant et al. 2008; Lagerloef et al. 2010; Vernieres et al.
432 2014). For salinity, this is particularly true in regions near the coastline where surface salinity is
433 heavily constrained by river runoff (Domingues et al. 2015; Tranchant et al. 2008; Vernieres et al.
434 2014). It has been demonstrated that assimilating satellite salinity observations can significantly
435 improve estimates of the upper-ocean state (Köhl et al. 2014; Toyoda et al. 2015; Vinogradova
436 et al. 2019; Martin et al. 2019) and the climate of the Indo-Pacific region, including El Niño and
437 Southern Oscillation (Hackert et al. 2014, 2019). Thus, besides their use in statistical RI models,
438 satellite salinity could potentially improve ocean analyses used to initialize dynamical TC forecast
439 models. Note that the results from the prediction model presented in this study are based on 'perfect
440 predictors' that are calculated from reanalyses in a 'hindcast' mode. Though the results are very
441 encouraging, further testing is required using realtime satellite and analysis data that are directly
442 used in forecasts. We propose a study, along the lines of a Joint Hurricane Testbed, to further this
443 cause and aid in the process of integrating salinity into operational RI forecasts.

444 *Data availability statement.* The sources for various data used in this study are provided in section
445 2a.

446 *Acknowledgments.* K. B. and L. R. L. were supported by the Office of Science (BER), U.S.
447 Department of Energy as part of the Regional and Global Modeling and Analysis (RGMA) Program.
448 The Pacific Northwest National Laboratory is operated for DOE by Battelle Memorial Institute
449 under contract DE-AC05-76RL01830. G. F. was funded by base funds to NOAA/AOML's Physical
450 Oceanography Division. K. B. and G. F. also acknowledge support from NOAA's Climate Program
451 Office, Climate Monitoring Program (Award Number: NA17OAR4310155). The various data used
452 in this study are freely available for download from the sources provided in section 2.

453 **References**

- 454 Androulidakis, Y., V. Kourafalou, G. Halliwell, M. Le Hénaff, H. Kang, M. Mehari, and R. Atlas,
455 2016: Hurricane interaction with the upper ocean in the amazon-orinoco plume region. *Ocean*
456 *Dynamics*, **66 (12)**, 1559–1588.
- 457 Avila, L. A., 2019: The 2018 atlantic hurricane season: Another catastrophic year for the united
458 states. *Weatherwise*, **72 (4)**, 14–21.
- 459 Baker, D. J., M. Glackin, S. J. Roberts, R. W. Schmitt, E. S. Twigg, D. J. Vimont, and R. A. Weller,
460 2019: The challenge of sustaining ocean observations. *Frontiers in Marine Science*, **6**, 105.
- 461 Balaguru, K., P. Chang, R. Saravanan, L. R. Leung, Z. Xu, M. Li, and J.-S. Hsieh, 2012: Ocean
462 barrier layers' effect on tropical cyclone intensification. *Proceedings of the National Academy*
463 *of Sciences*, **109 (36)**, 14 343–14 347.

- 464 Balaguru, K., G. R. Foltz, and L. R. Leung, 2018: Increasing magnitude of hurricane rapid
465 intensification in the central and eastern tropical atlantic. *Geophysical Research Letters*, **45 (9)**,
466 4238–4247.
- 467 Balaguru, K., G. R. Foltz, L. R. Leung, E. D. Asaro, K. A. Emanuel, H. Liu, and S. E. Zedler,
468 2015: Dynamic potential intensity: An improved representation of the ocean’s impact on tropical
469 cyclones. *Geophysical Research Letters*, **42 (16)**, 6739–6746.
- 470 Bender, M. A., and I. Ginis, 2000: Real-case simulations of hurricane–ocean interaction using a
471 high-resolution coupled model: Effects on hurricane intensity. *Monthly Weather Review*, **128 (4)**,
472 917–946.
- 473 Boutin, J., J. Vergely, and S. Marchand, 2017: Smos sss l3 debias v2 maps generated by catds cec
474 locean. *SEANOE*.
- 475 Carton, J. A., G. A. Chepurin, and L. Chen, 2018: Soda3: A new ocean climate reanalysis. *Journal*
476 *of Climate*, **31 (17)**, 6967–6983.
- 477 Chassignet, E. P., H. E. Hurlburt, O. M. Smedstad, G. R. Halliwell, P. J. Hogan, A. J. Wallcraft,
478 R. Baraille, and R. Bleck, 2007: The hycom (hybrid coordinate ocean model) data assimilative
479 system. *Journal of Marine Systems*, **65 (1-4)**, 60–83.
- 480 Cione, J. J., and E. W. Uhlhorn, 2003: Sea surface temperature variability in hurricanes: Implica-
481 tions with respect to intensity change. *Monthly Weather Review*, **131 (8)**.
- 482 DeMaria, M., 1987: Tropical cyclone track prediction with a barotropic spectral model. *Monthly*
483 *Weather Review*, **115 (10)**, 2346–2357.

- 484 DeMaria, M., M. Mainelli, L. K. Shay, J. A. Knaff, and J. Kaplan, 2005: Further improvements
485 to the statistical hurricane intensity prediction scheme (ships). *Weather and Forecasting*, **20** (4),
486 531–543.
- 487 Domingues, R., and Coauthors, 2015: Upper ocean response to hurricane gonzalo (2014): Salinity
488 effects revealed by targeted and sustained underwater glider observations. *Geophysical Research*
489 *Letters*, **42** (17), 7131–7138.
- 490 Durack, P. J., T. Lee, N. T. Vinogradova, and D. Stammer, 2016: Keeping the lights on for global
491 ocean salinity observation. *Nature Climate Change*, **6** (3), 228.
- 492 Emanuel, K., 2017: Will global warming make hurricane forecasting more difficult? *Bulletin of*
493 *the American Meteorological Society*, **98** (3), 495–501.
- 494 Emanuel, K. A., 1999: Thermodynamic control of hurricane intensity. *Nature*, **401** (6754), 665.
- 495 Gall, R., J. Franklin, F. Marks, E. N. Rappaport, and F. Toepfer, 2013: The hurricane forecast
496 improvement project. *Bulletin of the American Meteorological Society*, **94** (3), 329–343.
- 497 Goni, G. J., and J. A. Trinanes, 2003: Ocean thermal structure monitoring could aid in the intensity
498 forecast of tropical cyclones. *Eos, Transactions American Geophysical Union*, **84** (51), 573–578.
- 499 Grodsky, S. A., and Coauthors, 2012: Haline hurricane wake in the amazon/orinoco plume:
500 Aquarius/sacd and smos observations. *Geophysical Research Letters*, **39** (20).
- 501 Hackert, E., A. J. Busalacchi, and J. Ballabrera-Poy, 2014: Impact of aquarius sea surface salinity
502 observations on coupled forecasts for the tropical indo-pacific ocean. *Journal of Geophysical*
503 *Research: Oceans*, **119** (7), 4045–4067.

504 Hackert, E. C., R. M. Kovach, A. J. Busalacchi, and J. Ballabrera-Poy, 2019: Impact of aquarius and
505 smap satellite sea surface salinity observations on coupled el niño/southern oscillation forecasts.
506 *Journal of Geophysical Research: Oceans*, **124** (7), 4546–4556.

507 Hlywiak, J., and D. S. Nolan, 2019: The influence of oceanic barrier layers on tropical cyclone
508 intensity as determined through idealized, coupled numerical simulations. *Journal of Physical*
509 *Oceanography*, **49**, 1723–1745.

510 Kaplan, J., and M. DeMaria, 2003: Large-scale characteristics of rapidly intensifying tropical
511 cyclones in the north atlantic basin. *Weather and forecasting*, **18** (6), 1093–1108.

512 Kaplan, J., M. DeMaria, and J. A. Knaff, 2010: A revised tropical cyclone rapid intensification
513 index for the atlantic and eastern north pacific basins. *Weather and forecasting*, **25** (1), 220–241.

514 Kaplan, J., and Coauthors, 2015: Evaluating environmental impacts on tropical cyclone rapid
515 intensification predictability utilizing statistical models. *Weather and Forecasting*, **30** (5), 1374–
516 1396.

517 Klotzbach, P. J., C. J. Schreck III, J. M. Collins, M. M. Bell, E. S. Blake, and D. Roache, 2018:
518 The extremely active 2017 north atlantic hurricane season. *Monthly Weather Review*, **146** (10),
519 3425–3443.

520 Köhl, A., M. Sena Martins, and D. Stammer, 2014: Impact of assimilating surface salinity from
521 smos on ocean circulation estimates. *Journal of Geophysical Research: Oceans*, **119** (8), 5449–
522 5464.

523 Kowch, R., and K. Emanuel, 2015: Are special processes at work in the rapid intensification of
524 tropical cyclones? *Monthly Weather Review*, **143** (3), 878–882.

525 Lagerloef, G., and Coauthors, 2010: Resolving the global surface salinity field and variations by
526 blending satellite and in situ observations. *OceanObs 09*, European Space Agency, 587–597.

527 Landsea, C. W., and J. L. Franklin, 2013: Atlantic hurricane database uncertainty and presentation
528 of a new database format. *Monthly Weather Review*, **141** (10), 3576–3592.

529 Lee, C.-Y., M. K. Tippett, A. H. Sobel, and S. J. Camargo, 2016: Rapid intensification and the
530 bimodal distribution of tropical cyclone intensity. *Nature communications*, **7**, 10 625.

531 Lin, I.-I., G. J. Goni, J. A. Knaff, C. Forbes, and M. Ali, 2013: Ocean heat content for tropical
532 cyclone intensity forecasting and its impact on storm surge. *Natural hazards*, **66** (3), 1481–1500.

533 Lloyd, I. D., and G. A. Vecchi, 2011: Observational evidence for oceanic controls on hurricane
534 intensity. *Journal of Climate*, **24** (4), 1138–1153.

535 Mainelli, M., M. DeMaria, L. K. Shay, and G. Goni, 2008: Application of oceanic heat content
536 estimation to operational forecasting of recent atlantic category 5 hurricanes. *Weather and*
537 *Forecasting*, **23** (1), 3–16.

538 Martin, M. J., R. R. King, J. While, and A. B. Aguiar, 2019: Assimilating satellite sea-surface
539 salinity data from smos, aquarius and smap into a global ocean forecasting system. *Quarterly*
540 *Journal of the Royal Meteorological Society*, **145** (719), 705–726.

541 Newinger, C., and R. Toumi, 2015: Potential impact of the colored amazon and orinoco plume on
542 tropical cyclone intensity. *Journal of Geophysical Research: Oceans*, **120** (2), 1296–1317.

543 Pailler, K., B. Bourlès, and Y. Gouriou, 1999: The barrier layer in the western tropical atlantic
544 ocean. *Geophysical Research Letters*, **26** (14), 2069–2072.

545 Price, J. F., 1981: Upper ocean response to a hurricane. *Journal of Physical Oceanography*, **11** (2),
546 153–175.

- 547 Price, J. F., 2009: Metrics of hurricane-ocean interaction: vertically-integrated or vertically-
548 averaged ocean temperature? *Ocean Science*, **5** (3), 351–368.
- 549 Price, J. F., R. A. Weller, and R. Pinkel, 1986: Diurnal cycling: Observations and models of the
550 upper ocean response to diurnal heating, cooling, and wind mixing. *Journal of Geophysical*
551 *Research: Oceans*, **91** (C7), 8411–8427.
- 552 Rahmstorf, S., 2017: Rising hazard of storm-surge flooding. *Proceedings of the National Academy*
553 *of Sciences*, 201715895.
- 554 Reul, N., Y. Quilfen, B. Chapron, S. Fournier, V. Kudryavtsev, and R. Sabia, 2014: Multisen-
555 sor observations of the amazon-orinoco river plume interactions with hurricanes. *Journal of*
556 *Geophysical Research: Oceans*, **119** (12), 8271–8295.
- 557 Rozoff, C. M., and J. P. Kossin, 2011: New probabilistic forecast models for the prediction of
558 tropical cyclone rapid intensification. *Weather and Forecasting*, **26** (5), 677–689.
- 559 Rudzin, J. E., L. K. Shay, and B. Jaimes de la Cruz, 2019: The impact of the amazon–orinoco river
560 plume on enthalpy flux and air–sea interaction within caribbean sea tropical cyclones. *Monthly*
561 *Weather Review*, **147** (3), 931–950.
- 562 Sena Martins, M., N. Serra, and D. Stammer, 2015: Spatial and temporal scales of sea surface
563 salinity variability in the atlantic ocean. *Journal of Geophysical Research: Oceans*, **120** (6),
564 4306–4323.
- 565 Shay, L. K., and J. K. Brewster, 2010: Oceanic heat content variability in the eastern pacific ocean
566 for hurricane intensity forecasting. *Monthly Weather Review*, **138** (6), 2110–2131.
- 567 Shay, L. K., G. J. Goni, and P. G. Black, 2000: Effects of a warm oceanic feature on hurricane
568 opal. *Monthly Weather Review*, **128** (5), 1366–1383.

- 569 Stewart, S. R., 2017: Hurricane matthew (al142016) 28 september–9 october 2016. *National*
570 *Hurricane Center Tropical Cyclone Report, National Hurricane Center, Miami, Florida.*
- 571 Toyoda, T., and Coauthors, 2015: Improvements to a global ocean data assimilation system through
572 the incorporation of aquarius surface salinity data. *Quarterly Journal of the Royal Meteorological*
573 *Society*, **141 (692)**, 2750–2759.
- 574 Tranchant, B., C.-E. Testut, L. Renault, N. Ferry, F. Birol, and P. Brasseur, 2008: Expected impact
575 of the future smos and aquarius ocean surface salinity missions in the mercator ocean opera-
576 tional systems: New perspectives to monitor ocean circulation. *Remote Sensing of Environment*,
577 **112 (4)**, 1476–1487.
- 578 Vernieres, G., R. Kovach, C. Keppenne, S. Akella, L. Brucker, and E. Dinnat, 2014: The impact of
579 the assimilation of aquarius sea surface salinity data in the geos ocean data assimilation system.
580 *Journal of Geophysical Research: Oceans*, **119 (10)**, 6974–6987.
- 581 Vincent, E. M., K. A. Emanuel, M. Lengaigne, J. Vialard, and G. Madec, 2014: Influence of
582 upper ocean stratification interannual variability on tropical cyclones. *Journal of Advances in*
583 *Modeling Earth Systems*, **6 (3)**, 680–699.
- 584 Vincent, E. M., M. Lengaigne, J. Vialard, G. Madec, N. C. Jourdain, and S. Masson, 2012:
585 Assessing the oceanic control on the amplitude of sea surface cooling induced by tropical
586 cyclones. *Journal of Geophysical Research: Oceans*, **117 (C5)**.
- 587 Vinogradova, N., and Coauthors, 2019: Satellite salinity observing system: Recent discoveries
588 and the way forward. *Frontiers in Marine Science*, **6**, 243.
- 589 Wilks, D. S., 2011: *Statistical methods in the atmospheric sciences*, Vol. 100. Academic press.

- 590 Yan, Y., L. Li, and C. Wang, 2017: The effects of oceanic barrier layer on the upper ocean response
591 to tropical cyclones. *Journal of Geophysical Research: Oceans*, **122** (6), 4829–4844.
- 592 Yu, L., X. Jin, and R. Weller, 2008: Multidecade global flux datasets from the objectively analyzed
593 air-sea fluxes (oafux) project: Latent and sensible heat fluxes, ocean evaporation, and related
594 surface meteorological variables. *OAFlux Project Technical Report. OA-2008-01, 64pp.*

595 **LIST OF TABLES**

596 **Table 1. Estimating the significance of salinity for RI prediction in the North At-**
597 **lantic.** Results based on Logistic Model experiments. The first set of results
598 (rows 1 and 2) are for the period 2004–2015 using SSS from HYCOM ocean
599 reanalysis. The second set of results (rows 3 and 4) are for the period 2010–
600 2017 using SSS from SMOS. The domain of analysis is the eastern region. In
601 each set, the first row contains average skill scores for the model based on the
602 SHIPS-RII predictors only. The second row contains the average scores for
603 the model with SSS as an additional predictor. Values in bold indicate that
604 the improvement in model obtained by the addition of salinity is statistically
605 significant at the 95% level based on the respective scores. 29

606 TABLE 1. **Estimating the significance of salinity for RI prediction in the North Atlantic.** Results based
607 on Logistic Model experiments. The first set of results (rows 1 and 2) are for the period 2004–2015 using SSS
608 from HYCOM ocean reanalysis. The second set of results (rows 3 and 4) are for the period 2010–2017 using
609 SSS from SMOS. The domain of analysis is the eastern region. In each set, the first row contains average skill
610 scores for the model based on the SHIPS-RII predictors only. The second row contains the average scores for the
611 model with SSS as an additional predictor. Values in bold indicate that the improvement in model obtained by
612 the addition of salinity is statistically significant at the 95% level based on the respective scores.

	POD	FAR	AUROC	BS
SHIPS-RII	0.35	0.89	0.58	0.19
SHIPS-RII + SSS (HYCOM)	0.44	0.85	0.62	0.18
SHIPS-RII	0.53	0.77	0.70	0.18
SHIPS-RII + SSS (SMOS)	0.58	0.74	0.71	0.17

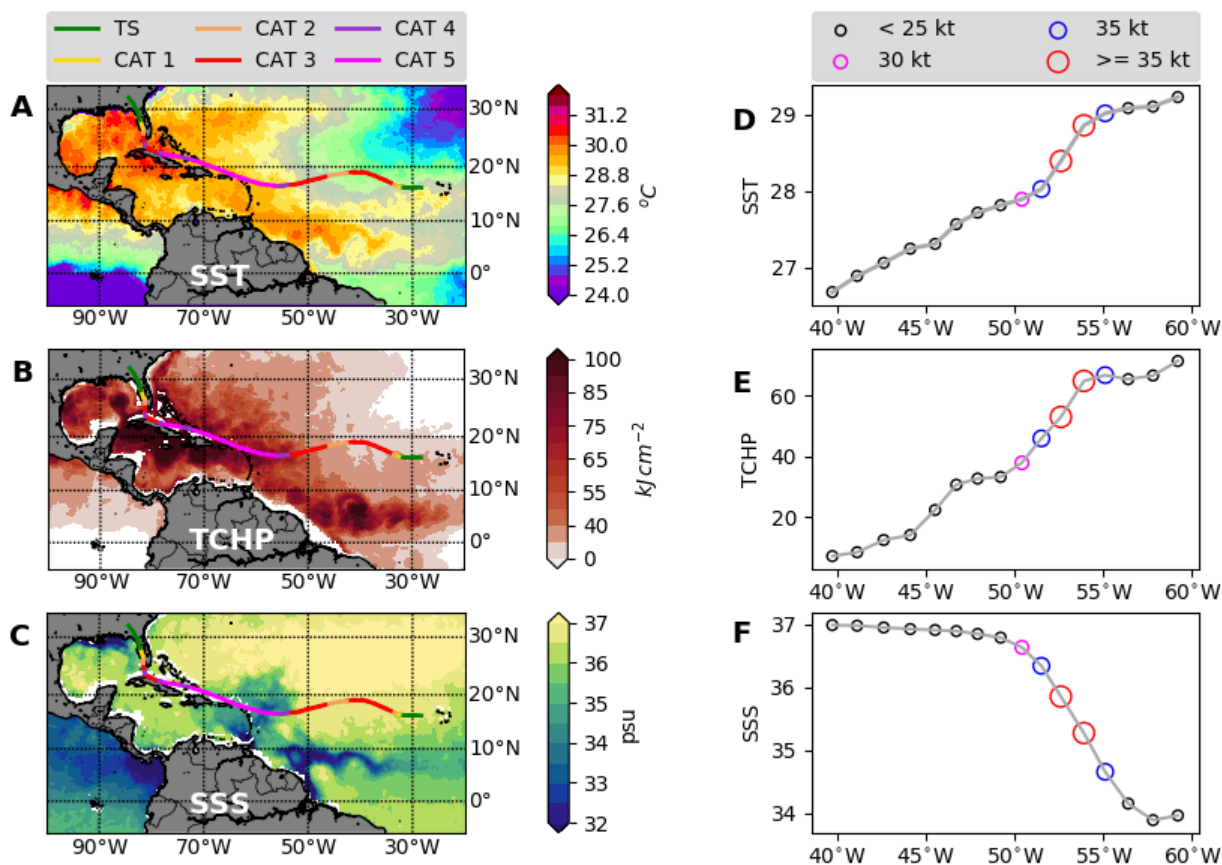
613 **LIST OF FIGURES**

614 **Fig. 1.** A) SST ($^{\circ}\text{C}$) and B) TCHP (kJ cm^{-2}) on 29 August, and C) SSS (psu) averaged between 19
 615 and 27 August, with the track of TC Irma (2017), color-coded by its intensity, overlaid. The
 616 legend shown above (A) corresponds to the strength of Irma based on the Saffir-Simpson
 617 scale. SST is from the satellite-based REMSS product, TCHP is based on HYCOM, and SSS
 618 is obtained from SMOS satellite. Along-track D) SST ($^{\circ}\text{C}$), E) TCHP (kJ cm^{-2}), and F) SSS
 619 (psu) for TC Irma. The circles in panels D, E and F represent the 24-hr intensity change at
 620 various 6-hr locations, with black denoting non-RI and color denoting RI. The legend shown
 621 above (D) corresponds to the magnitude of 24-hr intensity change experienced by Irma . . . 31

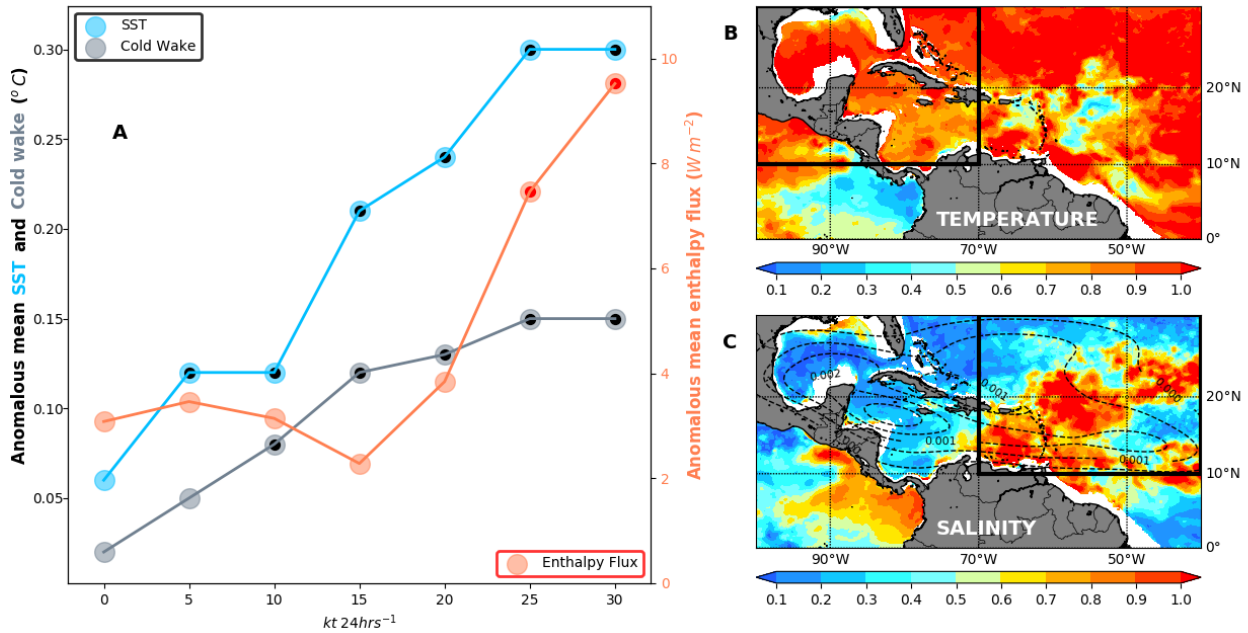
622 **Fig. 2.** A) Anomalous mean pre-storm SST (blue), cold wake (gray), and surface enthalpy flux (red)
 623 for Atlantic TCs as a function of intensification threshold. Anomalous mean represents the
 624 mean over all locations where the intensification rate exceeds a value minus the mean over
 625 all locations. While the total sample size is 2674, sample sizes for various intensification
 626 thresholds are as follows: 1641 (0 kt 24 hrs^{-1}), 1305 (5 kt 24 hrs^{-1}), 988 (10 kt 24 hrs^{-1}), 709
 627 (15 kt 24 hrs^{-1}), 493 (20 kt 24 hrs^{-1}), 307 (25 kt 24 hrs^{-1}), 205 (30 kt 24 hrs^{-1}). Concentric
 628 smaller dark circles indicate significance at the 95% level. B) Coefficient of linear regression
 629 between density stratification and temperature stratification at a depth of 100 m. C) Same as
 630 B) except for salinity stratification. Density, temperature, and salinity stratification have been
 631 normalized by subtracting their respective means and dividing by their standard deviations.
 632 Dashed contours in C) show the locations of RI. The boxes approximately represent the
 633 sub-regions used for the analysis shown in Figure 3. SST is from the satellite-based REMSS
 634 product, enthalpy flux is based on OAFflux, and ocean stratification (density, temperature and
 635 salinity) is calculated from HYCOM. . . . 32

636 **Fig. 3.** Anomalous mean TCHP (10 kJ cm^{-2}), temperature stratification (TSTRAT, $^{\circ}\text{C}$), density
 637 stratification (DSTRAT, kg m^{-3}), salinity stratification (SSTRAT, psu) and SSS (psu) in the
 638 western region (A and B) and in the eastern region (C and D) for cases where the 24-hr
 639 intensity change is greater than or equal to 5 kt (A and C) and RI (B and D). Anomalous
 640 mean represents the mean over all locations where the intensification rate exceeds a value
 641 minus the mean over all locations. The western region corresponds to 70°W – 100°W , 10°N –
 642 30°N and the eastern region corresponds to 40°W – 70°W , 10°N – 30°N . For each parameter,
 643 when the mean of the sub-sampled data is statistically different from the total mean at the
 644 95% level, it is indicated with hatching. TCHP, ocean stratification (DSTRAT, TSTRAT and
 645 SSTRAT), and SSS are based on HYCOM. . . . 33

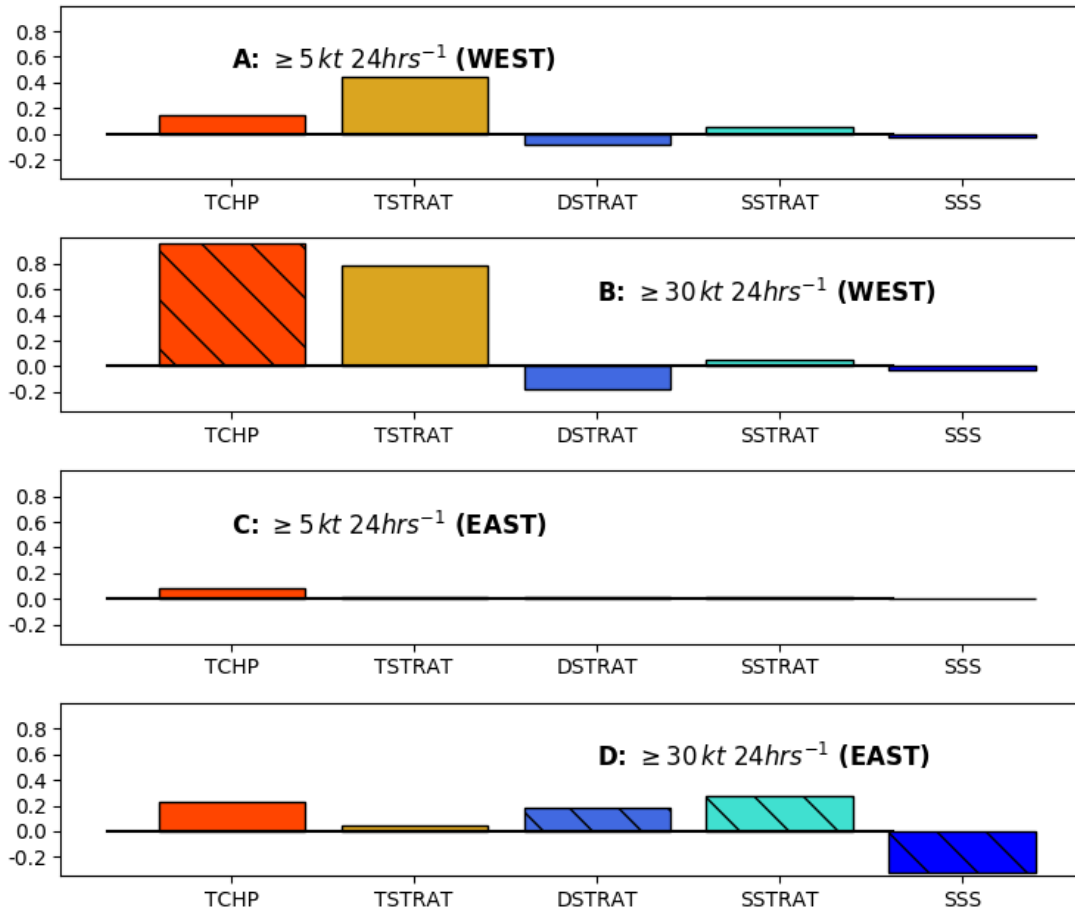
646 **Fig. 4.** A) Shaded: September mean surface salinity from SMOS. Colored squares: locations of
 647 Argo temperature and salinity profiles used to initialize the one-dimensional PWP model.
 648 B) Subsurface salinity from the floats at locations shown in A). C) Zonal wind stress used to
 649 force the PWP model (meridional wind stress is always zero). For the control experiment,
 650 a maximum wind speed of 60 kt was used (green). Other colors show profiles for which
 651 the wind speed was either linearly increased (purple, black) or decreased (blue, red) to reach
 652 wind speed indicated in the legend at the second radius of maximum wind (see Methods
 653 for details). D) Results from the model experiments, showing difference in SST cooling
 654 between the simulations with full salinity and constant salinity (positive values indicate
 655 reduced cooling due to salinity stratification). The colors correspond to those of the wind
 656 profiles in C) and shading indicates one standard error of the 20-member ensemble. . . . 34



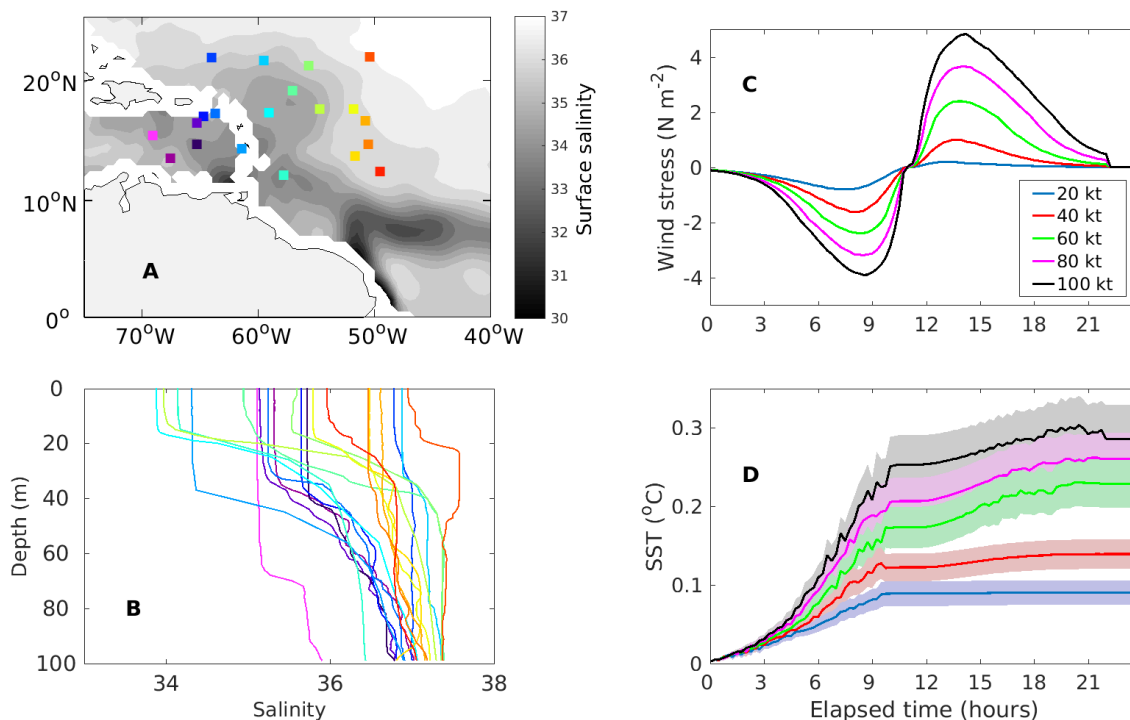
657 FIG. 1. A) SST ($^{\circ}\text{C}$) and B) TCHP (kJ cm^{-2}) on 29 August, and C) SSS (psu) averaged between 19 and 27
 658 August, with the track of TC Irma (2017), color-coded by its intensity, overlaid. The legend shown above (A)
 659 corresponds to the strength of Irma based on the Saffir-Simpson scale. SST is from the satellite-based REMSS
 660 product, TCHP is based on HYCOM, and SSS is obtained from SMOS satellite. Along-track D) SST ($^{\circ}\text{C}$), E)
 661 TCHP (kJ cm^{-2}), and F) SSS (psu) for TC Irma. The circles in panels D, E and F represent the 24-hr intensity
 662 change at various 6-hr locations, with black denoting non-RI and color denoting RI. The legend shown above
 663 (D) corresponds to the magnitude of 24-hr intensity change experienced by Irma



664 FIG. 2. A) Anomalous mean pre-storm SST (blue), cold wake (gray), and surface enthalpy flux (red) for
 665 Atlantic TCs as a function of intensification threshold. Anomalous mean represents the mean over all locations
 666 where the intensification rate exceeds a value minus the mean over all locations. While the total sample size
 667 is 2674, sample sizes for various intensification thresholds are as follows: 1641 (0 kt 24 hrs⁻¹), 1305 (5 kt 24
 668 hrs⁻¹), 988 (10 kt 24 hrs⁻¹), 709 (15 kt 24 hrs⁻¹), 493 (20 kt 24 hrs⁻¹), 307 (25 kt 24 hrs⁻¹), 205 (30 kt 24
 669 hrs⁻¹). Concentric smaller dark circles indicate significance at the 95% level. B) Coefficient of linear regression
 670 between density stratification and temperature stratification at a depth of 100 m. C) Same as B) except for
 671 salinity stratification. Density, temperature, and salinity stratification have been normalized by subtracting their
 672 respective means and dividing by their standard deviations. Dashed contours in C) show the locations of RI.
 673 The boxes approximately represent the sub-regions used for the analysis shown in Figure 3. SST is from the
 674 satellite-based REMSS product, enthalpy flux is based on OAFflux, and ocean stratification (density, temperature
 675 and salinity) is calculated from HYCOM.



676 FIG. 3. Anomalous mean TCHP (10 kJ cm^{-2}), temperature stratification (TSTRAT, $^{\circ}\text{C}$), density stratification
 677 (DSTRAT, kg m^{-3}), salinity stratification (SSTRAT, psu) and SSS (psu) in the western region (A and B) and in
 678 the eastern region (C and D) for cases where the 24-hr intensity change is greater than or equal to 5 kt (A and C)
 679 and RI (B and D). Anomalous mean represents the mean over all locations where the intensification rate exceeds
 680 a value minus the mean over all locations. The western region corresponds to 70°W – 100°W , 10°N – 30°N and the
 681 eastern region corresponds to 40°W – 70°W , 10°N – 30°N . For each parameter, when the mean of the sub-sampled
 682 data is statistically different from the total mean at the 95% level, it is indicated with hatching. TCHP, ocean
 683 stratification (DSTRAT, TSTRAT and SSTRAT), and SSS are based on HYCOM.



684 FIG. 4. A) Shaded: September mean surface salinity from SMOS. Colored squares: locations of Argo
 685 temperature and salinity profiles used to initialize the one-dimensional PWP model. B) Subsurface salinity from
 686 the floats at locations shown in A). C) Zonal wind stress used to force the PWP model (meridional wind stress is
 687 always zero). For the control experiment, a maximum wind speed of 60 kt was used (green). Other colors show
 688 profiles for which the wind speed was either linearly increased (purple, black) or decreased (blue, red) to reach
 689 wind speed indicated in the legend at the second radius of maximum wind (see Methods for details). D) Results
 690 from the model experiments, showing difference in SST cooling between the simulations with full salinity and
 691 constant salinity (positive values indicate reduced cooling due to salinity stratification). The colors correspond
 692 to those of the wind profiles in C) and shading indicates one standard error of the 20-member ensemble.

Supplemental material for “Pronounced impact of salinity on rapidly intensifying tropical cyclones”

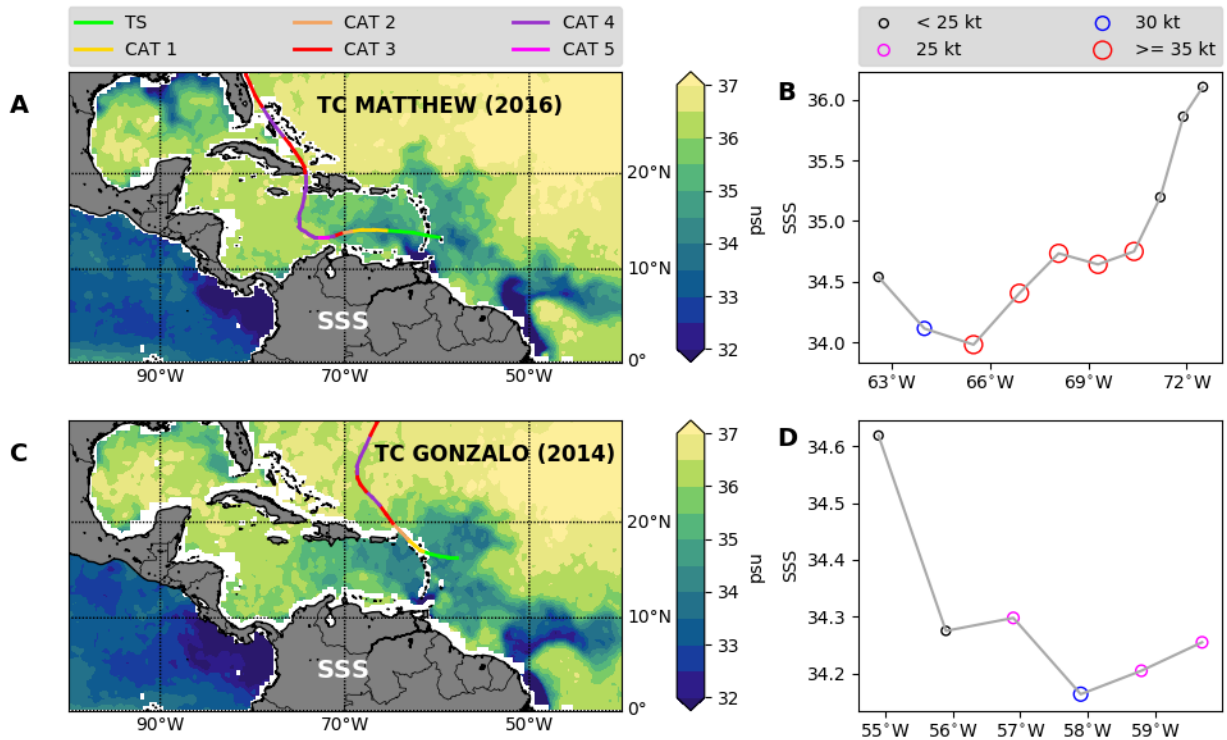


Figure 1: A) SSS (psu) averaged between 17 and 25 September, 2016 from SMOS with the track of TC Matthew, color-coded by its intensity, overlaid. B) Along-track SSS (psu) for Matthew. C) SSS (psu) averaged between 2 and 10 October, 2014 from SMOS with the track of TC Gonzalo overlaid. D) Along-track SSS (psu) for Gonzalo. The circles in panels B and D represent the 24-hr intensity change at various locations, with black denoting non-RI and color denoting RI. The legend shown above (A) corresponds to the strength of the TCs based on the Saffir-Simpson scale. The legend shown above (D) corresponds to the magnitude of 24-hr intensity change experienced by the TCs

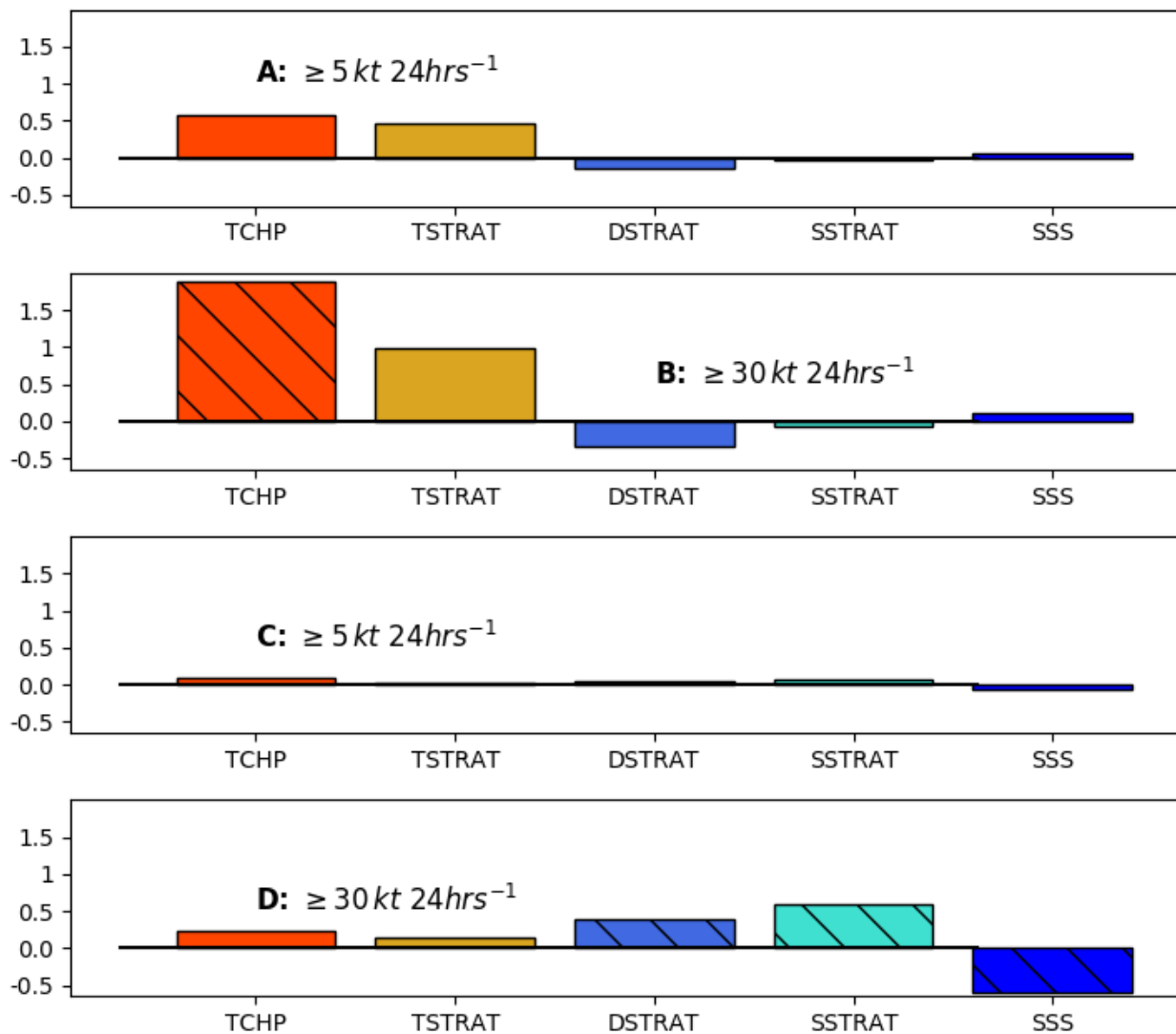


Figure 2: Anomalous mean TCHP (kJ cm^{-2}), temperature stratification (TSTRAT, $^{\circ}\text{C}$), density stratification (DSTRAT, kg m^{-3}), salinity stratification (SSTRAT, psu) and SSS (psu) in the western region (A and B) and in the eastern region (C and D) for cases where the 24-hr intensity change is greater than or equal to 5 kt (A and C) and RI (B and D). The western region corresponds to 70°W – 100°W , 10°N – 30°N and the eastern region corresponds to 40°W – 70°W , 10°N – 30°N . For each parameter, when the mean of the sub-sampled data is statistically different from the total mean at the 95% level, it is indicated with hatching. Analysis based on SODA ocean reanalysis.

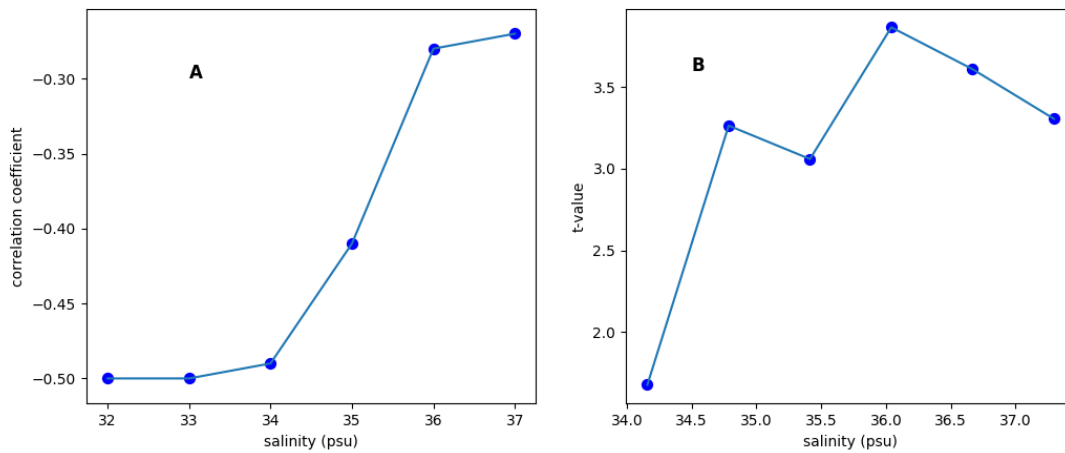


Figure 3: A) Correlation between SSS and upper-ocean density stratification for various salinity thresholds. For each value of threshold, data are considered only where SSS exceeds that value. SSS and ocean stratification are based on HYCOM. B) t-value for the difference between means of SSS values for RI and non-RI locations. For each value on the x-axis, SSS values higher than that value are set to the maximum. SSS from SMOS is used for this analysis.